Structure and dynamics of acetonitrile: Molecular simulation and neutron scattering

Samuel R Cohen, Marie Plazanet, Stéphane Rols, David J Voneshen, John T Fourkas, Benoit Coasne

Structure and Dynamics of Acetonitrile: Molecular Simulation and Neutron Scattering

Samuel R. Cohen,[1,2] Marie Plazanet,[2,*] Stéphane Rols,[3]
David J. Voneshen,[4,5] John T. Fourkas,[1,6,7,8,*] and Benoit Coasne[2,*]

[1] Department of Chemistry & Biochemistry, University of Maryland, College Park, 20742 Maryland, United States

[2] Univ. Grenoble Alpes, CNRS, LIPhy, 38000 Grenoble, France

[3] Institut Laue-Langevin, 71 Avenue des Martyrs, 38042 Grenoble, France

[4] ISIS Facility, Rutherford Appleton Laboratory, Chilton, Didcot, Oxon OX11 0QX, United Kingdom

[5] Department of Physics, Royal Holloway University, London, Egham, TW20 0EX, United Kingdom

[6] Institute for Physical Science and Technology, University of Maryland, College Park, 20742 Maryland, United States

[7] Maryland NanoCenter, University of Maryland, College Park, 20742 Maryland, United States

[8] Maryland Quantum Materials Center, University of Maryland, College Park, 20742 Maryland, United States

* To whom correspondence should be sent. Marie Plazanet (marie.plazanet@univ-grenoble-alpes.fr), John T. Fourkas (fourkas@umd.edu), Benoit Coasne (benoit.coasne@univ-grenoble-alpes.fr)

Abstract

We examine the interplay between organization and dynamics in bulk liquid acetonitrile. Using angularly resolved radial distribution functions, $g(r,\theta)$, derived from molecular simulations, we identify a complex microscopic structure in which most liquid molecules are associated with one or more neighboring molecules in an antiparallel, "octupole-paired" configuration and/or an offset, head-to-tail configuration. A detailed analysis of these structural motifs reveals that the offset head-to-tail dimers are the most prevalent. A time-dependent pairing analysis corroborates this picture of robust molecular associations favoring head-to-tail dimers, which last longer than antiparallel dimers. This organization, which is associated with pairing times (~ps) longer than the typical rotational and translational time constants, cannot be explained on the basis of the Coulomb interactions in the dimer, and so must arise from collective effects that are neither strong nor specific. Finally, using both neutron-scattering techniques and molecular simulations, we study dynamics in liquid acetonitrile over time scales ranging from subpicosecond (the vibrational density of states) to picosecond (rotational/translational motions and the generalized density of states) to tens of picoseconds (self-diffusivity in the Fickian regime).

1. Introduction

Acetonitrile (methyl cyanide) is an aprotic organic molecule with a large, permanent dipole moment of 3.92 D [1]. The amphiphilic character of this molecule makes liquid acetonitrile (ACN) a good solvent for many dipolar and non-dipolar solutes. Accordingly, both neat ACN and its binary mixtures with water are commonly used as the solvent medium for reactions and separations [2,3]. ACN has also served, for several decades, as an important model system for the study of molecular liquids, due to the combination of its large dipole moment and its nonassociated character [4-45]. Despite the fact that ACN is a simple, small molecule that is aprotic, the liquid nevertheless exhibits unexpectedly complex behavior. Perhaps the most notable feature of this liquid is its short-range structure and strong orientational correlations [4-10]. The most commonly cited feature of this structure is the propensity for the cyano groups of neighboring molecules to align antiparallel to one another [4-7,46,59]. This behavior is often attributed to dipole-dipole interactions, although integral equation calculations [11-13] and molecular dynamics simulations [23] can reproduce the structure factors of this liquid without taking into account explicit attractive interactions, suggesting that the molecular shape plays a major role in this organization.

Many theoretical [11,13-19], molecular simulation [20-36], and experimental [4-10,37-45] studies have explored the intermolecular organization and dynamics of ACN. Despite many decades of investigation, there are important outstanding questions regarding the properties of the bulk liquid, particularly with regard to the details of its orientational ordering and the relationship of this ordering to dynamics and solvation. For example, it is not yet well understood how the organization about a molecule in the liquid state depends on intermolecular distance. Previous molecular simulations using three- and six-site models for ACN revealed oscillations in an orientational correlation function extending out to at least 10 Å from a central molecule, but these works focused solely on the relative orientation as a function of the distance from this molecule [23,33-35]. A more recent study applied a reverse Monte Carlo approach to X-ray and neutron diffraction data to explore the joint orientational and positional ordering in ACN [30].

The organization and dynamics of neat ACN at interfaces [47-49], in mesoporous media [50-55], and mixed with bulk [56-65] and interfacial [66-70] water are examples of topics of considerable

current interest that require a more detailed understanding of the microscopic properties of neat acetonitrile. These are some of the outstanding problems that have been a driving force in the active development, characterization, and comparison of force fields for liquid ACN [31-36,71-82]. With these issues in mind, we report the results of molecular simulations and neutron-scattering experiments on bulk ACN. We employ a widely-used and reliable force field [76] to undertake an in-depth characterization of this liquid's structure and dynamics. We also benchmark our results against experimental data from the literature and from our own inelastic and quasielastic neutron scattering studies.

In Section 2, we describe the technical details of the molecular simulations and neutron-scattering experiments. In Section 3, we present angularly resolved radial distribution functions, $g(r,\theta)$, which provide deeper insight into the organization of the liquid than is possible using conventional radial distribution functions. These two-dimensional distribution functions allow us to elucidate the details of the molecular associations among nearest-neighbor ACN molecules, which we divide into antiparallel and head-to-tail configurations. We then explore the connections between structure and dynamics by determining typical pairing times between acetonitrile molecules using the formalism of mean-first passages. We investigate additional dynamical properties of ACN, including different vibrational densities of states, which we discuss in light of our experimental results obtained via quasielastic and inelastic neutron scattering (self and collective diffusivity and generalized density of states). In Section 4, we give concluding remarks and directions for future work.

2. Computational and Experimental Methods

2.1. Molecular Simulation

2.1.1. Model

Liquid ACN was simulated using the flexible, 6-site, all-atom model developed by Nikitin and Lyubartsev [76], which has been shown to reproduce the density, the heat of evaporation, and the site-site radial distribution functions of this liquid accurately. The model also reproduces well the experimental values for the self-diffusion coefficient and the dielectric constant of the liquid. An ACN molecule, with the atom labels and partial charges used in this work, is shown in Fig. 1A. The non-bonded interactions are described via a pair potential given by

$$E_{non-bonded} = \sum_i \sum_{j \neq i} \left\{ 4\varepsilon_{ij} \left[\left(\frac{\sigma_{ij}}{r_{ij}} \right)^{12} - \left(\frac{\sigma_{ij}}{r_{ij}} \right)^{6} \right] + \frac{1}{4\pi\varepsilon_0} \frac{q_i q_j}{r_{ij}} \right\}. \quad (1)$$

This potential consists of 12-6 Lennard-Jones and Coulombic terms, where *i* and *j* are on different molecules, ε_{ij} and σ_{ij} are the Lennard-Jones parameters for the potential-well depth and characteristic site radius, respectively, r_{ij} is the separation distance between sites *i* and *j*, ε_0 is the permittivity of vacuum, and q_i and q_j are the charges on sites *i* and *j*, respectively. For atoms on the same molecule, the only non-bonded interactions considered are the 1,4 interactions. The 1,4 electrostatic interactions are scaled by a factor 0.83, and the 1,4 Lennard-Jones interactions are scaled by a factor 0.5. The energy E_{bonded} of the intramolecular terms is

$$E_{bonded} = \sum_{bonds} K_r (r - r_0)^2 + \sum_{angles} K_\theta (\theta - \theta_0)^2, \quad (2)$$

where K_r is the harmonic bond coefficient, r is the bond distance, r_0 is the equilibrium bond distance, K_θ is the harmonic angle coefficient, and θ_0 is the equilibrium value of angle θ. The CT-YC-YN θ_0 is 180˚, the HC-CT-YC θ_0 is 110˚, and the HC-CT-HC θ_0 is 109.5˚. The total energy of the system is the sum of the bonded and non-bonded energies. Long-range Coulombic interactions were included using Ewald summation with a precision of 10^{-5}. The cut-off distances for the Lennard-Jones interactions and the real-space part of the Ewald sum were both set to 14 Å. Fig. 1B shows a representative configuration from a simulation of the bulk liquid.

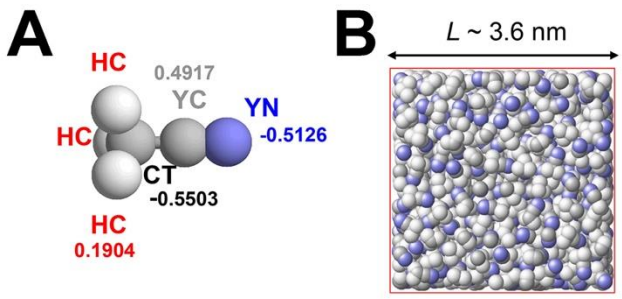

Fig. 1 (A) An acetonitrile molecule, showing the label and partial charge for each atom type. (B) Representative molecular configuration at T = 298 K for bulk liquid acetonitrile; the red frame indicates the molecular simulation box used in the calculations.

2.1.2. Molecular Dynamics Simulations

Molecular dynamics simulations were performed with LAMMPS [83] using the interaction potentials in Eqs. (1) and (2). The equations of motion were integrated with a time step of 1 fs. All of the initial configurations were built using PACKMOL [84], and the simulations were preceded by an energy minimization with an energy tolerance of 10^{-6}. The simulations for the bulk liquid used a 36 Å × 36 Å × 36 Å box with periodic boundary conditions. A simulation was performed to measure the density of the bulk liquid by equilibrating in the isothermal/isobaric (*NPT*) ensemble at 298 K and 1 bar for 200 ps using a Nosé-Hoover thermostat and barostat [85] with 30 fs and 1000 fs relaxation constants, respectively. Using the equilibrated systems, the simulation was then run in the *NPT* ensemble up to 2 ns. All other simulations were equilibrated in the *NVT* ensemble at 298 K for 200 ps using a Nosé-Hoover thermostat with a 30 fs relaxation constant. Using the equilibrated systems, the simulations were then run in the *NVE* ensemble up to 2 ns for the bulk liquid. Configurations were analyzed every 1 ps over the entire trajectory to calculate each angular heat map. For the calculation of the mean-squared displacements and mean first passage times, configurations were analyzed every 5 fs out to approximately 50 ps.

2.2. Neutron-Scattering Experiments

ACN (Honeywell Chromasolv™, HPLC-grade, > 99.9%) and ACN with deuterium/hydrogen substitution (Sigma Aldrich, ≥ 99.8 atom %D) were used in the experiments. Neutron-scattering measurements were performed at ISIS (UK) on the LET time-of-flight spectrometer. Based on the repetition-rate multiplication, energies of 1.78, 2.83, 5.18, 12.39, and 60.11 meV were selected

from the incoming beam. Scattered neutrons were monitored on detector banks covering the angular range from 5° to 135°. Because all incident energies gave consistent data, we present here only data recorded with E_i = 2.83 meV, which best cover the energy and q ranges of interest, enabling a resolution of 70 μeV for the elastic line. Data were reduced using standard routines included in Mantid [86], and fitting was performed in the Large-Array Manipulation Program (LAMP) [87].

2.2.1. Inelastic Neutron Scattering

Scattering involving energy transfers larger than ~1 meV that arises from a periodic excitation is considered to be inelastic. Scattering in such a process is not limited by any selection rules, and multiphonon processes occur. The double differential cross section of neutron scattering can be written as [88]

$$\left(\frac{d^2\sigma}{d\Omega d\omega}\right)_{inc} = \frac{k_f}{k_i}\sum_{\kappa}\frac{\sigma_{inc}(\kappa)}{8\pi m_{\kappa}}\sum_{j\in\{j_{\kappa}\}} e^{-2W_j(\vec{q})}\sum_i \frac{|\vec{q}.\vec{e}_i(j)|^2}{\omega_i}[(n(\omega_i)+1)\delta(\omega-\omega_i)]\,, \quad (3)$$

where k_i and k_f are the wave vectors of the incident and scattered neutrons, Ω is the scattering solid angle, ω is the angular frequency, $\vec{q}$ is the momentum transfer, $W(\vec{q})$ is the Debye-Waller factor, $n(\omega)$ is the Bose occupation factor, m the mass of the scattering atom, $\vec{e}_i(j)$ is the atom's displacement in vibrational mode i, and $\sigma_{inc}(\kappa)$ is the neutron incoherent scattering cross section of the atoms of type κ. For an isotropic and incoherent sample, one can simplify Eq. (3) to obtain [88]

$$\left(\frac{d^2\sigma}{d\Omega d\omega}\right)_{inc} = \frac{k_f}{k_i}\frac{q^2}{3}\sum_{\kappa}\frac{\sigma_{inc}(\kappa)}{8\pi m_{\kappa}}\sum_{j\in\{j_{\kappa}\}} e^{-2W_j(\vec{q})}\frac{g_j(\omega)}{\omega}(n(\omega)+1)\,, \quad (4)$$

where $\sigma_{inc}(\kappa)$ is the neutron incoherent scattering cross section, and $g_j(\omega)$ is the density of states of atom j of type κ for all the modes i

$$g_j(\omega) = \sum_i |\vec{e}_i(j)|^2\delta(\omega-\omega_i)\,. \quad (5)$$

Summing Eq. (4) over all atoms *j* and type κ, we obtain

$$\left(\frac{d^2\sigma}{d\Omega d\omega}\right)_{inc} = \frac{k_f}{k_i} q^2 \frac{N}{8\pi} e^{-2W(q)} \frac{G(\omega)}{\omega} (n(\omega) + 1) \,, \tag{6}$$

where $G(\omega)$ is the generalized density of states (GDOS) given by

$$G(\omega) = \sum_{\kappa=1}^{N} \frac{\sigma_{inc}(\kappa)}{m_\kappa} g_\kappa(\omega) \,, \tag{7}$$

and $g_\kappa(\omega)$ is the partial density of states for all of the atoms *N* of a given chemical species κ. The quantity $g_\kappa(\omega)$ is experimentally accessible using inelastic neutron scattering. In the case of ACN, the experimentally-derived GDOS is dominated by the hydrogen contribution. When H is replaced by D (ACN-d_3), one must invoke the so-called "incoherent approximation" [89] to derive $G(\omega)$. The use of this approximation necessitates averaging the coherent cross section over a large domain of momentum transfer, which is assured in our experiments by the use of a detector bank covering a large range of scattering angles.

2.2.2. Quasielastic Neutron Scattering

Quasielastic neutron scattering (QENS) refers to the symmetric broadening of the elastic line by the scattering of neutrons from diffusive excitations, such as rotational and translational dynamics. The QENS signal, from which $S(q,\omega)$ is extracted, can be sliced at constant q and described in a first approximation by a sum of Lorentzian functions

$$S(q,\omega) = e^{-2W(q)} \{\sum_i A_i(q) \times L_i(q,\omega)\} \otimes R(q,\omega) + b(q) \,, \tag{8}$$

where the $L_i(q,\omega)$ are the Lorentzian contribution to the QENS signal, the $A_i(q)$ are the corresponding amplitudes, $R(q,\omega)$ is the resolution function of the instrument, and $b(q)$ is the flat background. The widths and amplitudes of the Lorentzians as a function of q enable the determination of the rotational or translational nature of the dynamics.

We further refined the model using a sum of two terms describing molecular rotations convolved with the translational dynamics, so that we obtain

$$S(q,\omega) = exp\left(-\frac{\langle u^2\rangle q^2}{3}\right)[I(q)_{El}\delta(\omega) + S(q,\omega)_T \otimes S_1(q,\omega)_R + S(q,\omega)_T \otimes S_2(q,\omega)_R]\,, \quad (9)$$

where $\langle u^2\rangle$ is the mean-squared displacement and $I(q)_{El}$ is the remaining elastic peak arising from the sample holder. This latter feature was fitted with an elastic peak by multiplication with the delta function $\delta(\omega)$. The first and second rotational contributions correspond to the spinning and tumbling of the molecule. The translational contribution can be written as [90]

$$S(q,\omega)_T = \frac{1}{\pi}\frac{\Gamma_T}{\omega^2+\Gamma_T^2}\,, \quad (10)$$

where Γ_T is the half-width at half maximum of the translational Lorentzian function, and is defined as

$$\Gamma_T = \frac{D_T q^2}{1+\tau D_T q^2}\,, \quad (11)$$

where D_T is the self-diffusion constant and τ is the residence time. We assume isotropic rotational contributions such that the rotational contribution can be written as [90]

$$S(q,\omega)_R = A_0(q)\delta(\omega) + \sum_{i=1}^{\infty} A_i(q)\frac{1}{\pi}\frac{\Gamma_i}{(\omega)^2+\Gamma_i^2}\,, \quad (12)$$

with

$$A_i(q) = (2i+1)j_i^2(qR) \quad (13)$$

and

$$\Gamma_i = i(i+1)D_R\,, \quad (14)$$

where R is the radius of rotation. D_R is the isotropic rotational diffusion constant, which is related to the characteristic rotational time by $\tau_R = 1/(2D_R)$.

3. Results and Discussion

3.1. Structure

To compare the structure of the simulated liquid with experimental measurements, the total static structure factor $S(q)$ was calculated for three different ACN isotopologues, CH_3CN, $CD_3C^{15}N$, and $CD_3C^{14}N$. The total structure factor is proportional to the differential scattering cross-section that is measured in diffraction experiments. For a polyatomic system such as ACN, the total structure factor is essentially a weighted sum of the partial structure factors [91]. The partial structure factors $S_{\alpha\beta}(q)$ for N_{mol} molecules consisting of atoms α and β were calculated according to [92]

$$S_{\alpha\beta}(q) = \left\langle \frac{1}{N_{mol}} \rho_q^{\alpha} \rho_{-q}^{\beta} \right\rangle , \tag{15}$$

where ρ_q^{α} and ρ_{-q}^{β} are the Fourier components of the microscopic density,

$$\rho_q^{\alpha} = \sum_{i=1}^{N_{\alpha}} e^{-iq \cdot r_{\alpha,i}} \tag{16}$$

and

$$\rho_{-q}^{\beta} = \sum_{i=1}^{N_{\beta}} e^{iq \cdot r_{\beta,i}} \ , \tag{17}$$

for the numbers N_{α} and N_{β} of atoms in the system with position vectors $r_{\alpha,i}$ and $r_{\beta,i}$ for the *i*th atom of type α and β, respectively, and q is the magnitude of the scattering wave vector. The brackets in Eq. (15) denote an ensemble average. To obtain the total structure factor, the partial structure factors were multiplied by the corresponding neutron coherent scattering lengths $\overline{b}_{\alpha}$, $\overline{b}_{\beta}$ of each component according to

$$S(q) = \frac{\sum_{\alpha,\beta=1}^{6} \overline{b}_{\alpha} \overline{b}_{\beta} S_{\alpha\beta}(q)}{\sum_{\alpha=1}^{6} \overline{b}_{\alpha}^{\ 2}} , \tag{18}$$

where the choice of denominator normalizes the function to 1 at large q.

The simulated structure factors for the three isotopologues are plotted in Fig. 2, and the corresponding experimental static structure factors for $CD_3C^{15}N$ and $CD_3C^{14}N$ are shown for comparison. There is excellent agreement between the simulated and experimental static structure factors for these liquids. Note that we could not find any experimental results for CH_3CN in the literature, presumably because the strong incoherent background from the hydrogen atoms masks most of the signal. A sharp diffraction peak in the vicinity of q = 1.5 to 2 Å^{-1} is present in all cases, and is indicative of short-range order. However, it is difficult to interpret the structure factors

qualitatively beyond this observation. It is more informative to study pair correlations in real space via partial radial distribution functions.

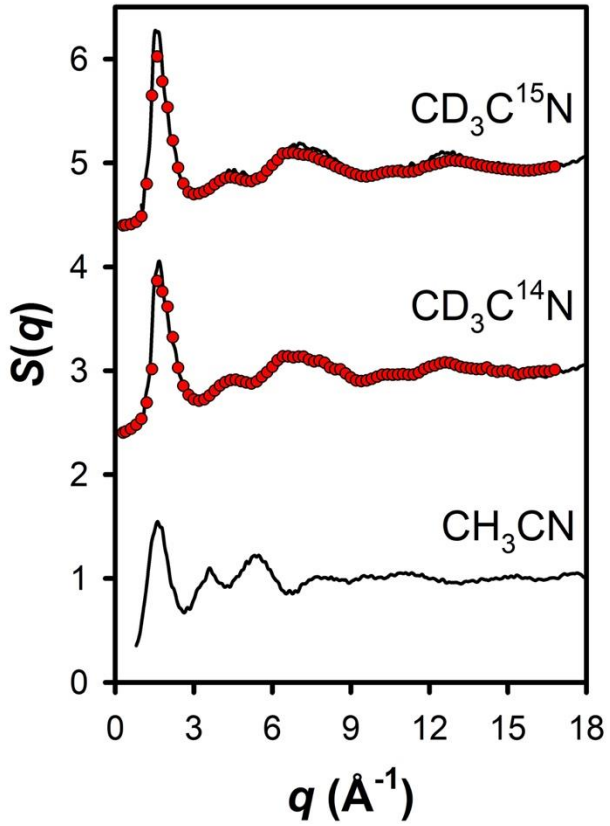

Fig. 2 Static structure factor $S(q)$ for bulk ACN at 298 K as obtained from molecular simulations (black) and neutron-diffraction experiments [8,9] (red), where q is the magnitude of the scattering wave vector. The three sets of data are for different isotopologues, with deuterium/hydrogen and/or $^{14}N/^{15}N$ isotopic substitutions. The $S(q)$ for the three different isotopologues are offset vertically for clarity.

The center-of-mass radial distribution function and partial radial distribution functions are shown in Fig. S1. In previous works, the partial radial distribution functions for ACN have been interpreted as being quite sensitive to the dipole-dipole interactions [13,23,33]. In contrast, the structure factors have been shown to be reproducible without taking attractive interactions into account explicitly [11,13,23], which led to the conclusion [12,13,33] that structure factors are not particularly sensitive to details of the intermolecular effects of electrostatic attractions. The subset of partial radial distribution functions shown in Fig. S1 that have been reported previously are essentially the same as in prior work using this force field [76], and all of the partial radial

distribution functions are similar to those reported for extensively-studied three- [33,34,73] and six-site [72,74] models and reverse Monte Carlo simulations [30].

To gain deeper insight into the orientational ordering of liquid ACN, we calculated angularly resolved radial distribution functions, $g(r,\theta)$. These functions are calculated by integrating in spherical coordinates over both r and θ:

$$g(r,\theta) = \frac{N(r,\theta)}{\langle\rho\rangle 2\pi \int_R^{R'} r^2 dr \int_\theta^{\theta'} sin\theta d\theta} \quad , \tag{19}$$

where $\langle\rho\rangle$ is the average density of the liquid. This formula is sometimes known in the literature as a cone correction [93], because the volume defined by a solid angle depends on the angle θ. Angularly resolved radial distribution functions give the probability that two ACN molecules with selected sites separated by a distance r make an angle θ. Here, θ is calculated from the dot product between unit vectors on different molecules, as determined using the CT-YN vector in the direction of YN on each molecule. In polyatomic liquids, $g(r,\theta)$ can be considerably more informative than a traditional radial distribution function [61,94,95]. In Fig. 3, we show $g(r,\theta)$ for the molecular center of mass, along with the corresponding $g(r)$. The center-of-mass $g(r,\theta)$ shows that there are two distinct populations contributing to $g(r)$ at short distances. The first peak in $g(r)$ arises from antiparallel pairs of molecules with a center-of-mass separation on the order of 3.7 Å (configuration 1 in Fig. 3). We note that these molecules are not dipole paired in the traditional sense in which this term is used for acetonitrile, in which the cyano groups of the two molecules interact with one another [4]. Rather, the molecules align as to allow for favorable interactions among all of the complementary partial charges on the atoms (see Fig. 1). For the sake of clarity, we will therefore refer to this motif as octupole pairing, although as we will see below, electrostatic interactions between the two molecules are not the primary driving force for this pairing. Similar dimer structures have been observed for liquid molecules with few near neighbors in simulations using a different force field [32] and in gas-phase dimers based on quantum-chemical calculations [96]. The second peak arises from a population of head-to-tail pairs with a broad distribution of angles centered around ~90° (configuration 2 in Fig. 3). Note that the area under this second peak is much larger than that under the first peak. The center-of-mass separation in the latter pairs decreases with increasing θ.

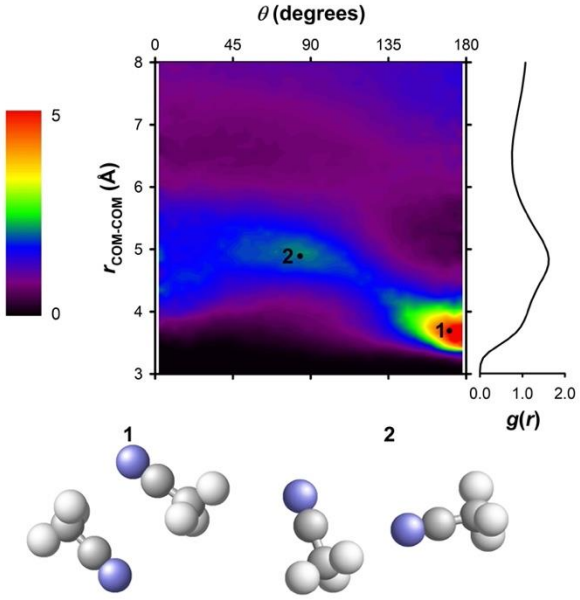

Fig. 3 The center-of-mass $g(r,\theta)$ and $g(r)$ for acetonitrile, along with representative configurations from the indicated regions.

As a further test of the reliability of the microscopic structure predicted by this force field, in Fig. S2 we compare our calculated distance-dependent, normalized angular probability distribution $g_{\text{CT-CT}}(r,\cos\theta)$ with that from the reverse Monte Carlo work of Pothoczki and Pusztai [30]. As shown in Fig. S2, our molecular simulation results are in good agreement with the reverse Monte Carlo results [30], which were obtained using the OPLS-AA [97] force field as a constraint. It is interesting to note that these two distinct numerical approaches lead to similar microscopic organization, despite being based on different hypotheses. Molecular dynamics relies purely on a force field, whereas reverse Monte Carlo consists of an error minimization between the experimental and simulated radial distribution functions. In particular, even though the reverse Monte Carlo calculations in [30] are further constrained by the use of the OPLS-AA force field, this force field differs from the one used in our molecular dynamics simulations, and so cannot be the source of the similarities. Reconstruction of a fully three-dimensional picture of a material from knowledge of lower-order correlation functions is a well-known inverse problem [98], and from this perspective it can be understood that one-dimensional structural functions, which give

pair information, under-constrain the problem of liquid structure. It is therefore not obvious that the microscopic organization in the two models should be the same, but the agreement between them gives us confidence in the ability of this force field to reveal structural and dynamic details in this liquid.

In Fig. 4, we show the angularly resolved radial distribution functions involving the physical centers of the methyl (Me) and cyano (CN) groups, i.e., $g_{\text{Me-Me}}(r,\theta)$, $g_{\text{Me-CN}}(r,\theta)$, and $g_{\text{CN-CN}}(r,\theta)$. The corresponding $g(r)$ is presented in each case for comparison. Our choice of these two functional groups was inspired by investigations into nanostructural organization in ionic liquids [99], and by molecular simulations [60,62] of acetonitrile/water mixtures that showed evidence of microheterogeneities when examining differences in the partial radial distribution function between the methyl group and the central carbon of ACN at different concentrations. These angularly resolved radial distribution functions provide a wealth of new information about the organization of this liquid.

The Me-Me partial radial distribution is broad and relatively featureless, suggesting that the methyl groups do not have a preference for specific directional interactions. However, $g_{\text{Me-Me}}(r,\theta)$ (Fig. 4) has regions of parallel (configuration 3), head-to-tail (configuration 4), and antiparallel (configuration 5) dimers. The first peak in $g(r)$ arises from a number of contributions. First, there is a region consisting of parallel dimers (configuration 3). There is also lobe in the distribution at a distance of approximately 5 Å arising from from offset, head-to-tail molecules

(configuration 4). The final major contribution is from roughly antiparallel, octupole-paired molecules (configuration 5).

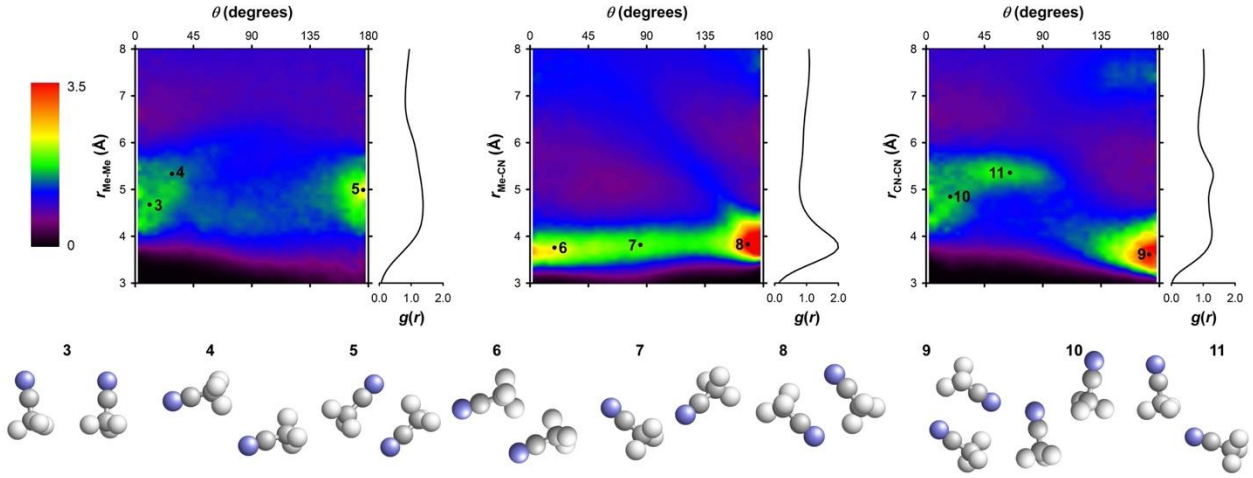

Fig. 4 Radial distribution functions and angularly resolved radial distribution functions for acetonitrile with respect to the methyl-methyl distance, the methyl-cyano distance, and the cyano-cyano distance for different molecules, with the angle θ defined as described in the text, along with representative configurations from the indicated regions.

The pronounced first peak in $g_{\text{Me-CN}}(r)$ is qualitatively similar to the first peak in $g_{\text{CT-YN}}(r)$ (Fig. 1A), which has been interpreted previously in simulations of both three- [33] and six-site [35] models of ACN to reflect the head-to-tail alignment of neighboring dipoles. The $g_{\text{Me-CN}}(r,\theta)$ in Fig. 4 instead reveals the presence of structures in which the nitrogen atom associates with a methyl group in an offset head-to-tail fashion, with angles ranging from small acute angles (configuration 6) to large acute angles (configuration 7) to octupole pairs (configuration 8). Even the pairs at small acute angles are dominated by offset, rather than true, head-to tail structures. Surprisingly, this is the most structured of the angularly-resolved radial distribution functions in Fig. 4, which suggests that bulk liquid acetonitrile does not feature polar and nonpolar nanodomains.

Based on previous work, $g_{\text{CN-CN}}(r)$ is expected to reflect dipole pairing of cyano groups [33]. However, the first feature of $g_{\text{CN-CN}}(r)$ exhibits two peaks. The corresponding angularly resolved radial distribution function (Fig. 4) demonstrates that these peaks correspond to two different types of local structures. The peak at shorter separations corresponds to antiparallel, octupole-paired

dimers (configuration 9), in which the nitrogen atom of one molecule is associated with a hydrogen atom of another molecule. Here, and in the other angularly resolved radial distribution functions, we find no evidence for a significant population of cyano dipole-paired dimers. The other dominant structural motif in liquid acetonitrile, head-to-tail dimers, is observed in all of the angularly resolved radial distribution functions shown here. In $g_{\text{CN-CN}}(r,\theta)$ in Fig. 4, the broad peak centered at ~5.3 Å arises from dimers in which one cyano group associates with a methyl group in an offset, head-to-tail fashion (configuration 10 and configuration 11).

To analyze the population of head-to-tail dimers, we isolated molecular pairs based on $g_{\text{Me-CN}}(r,\theta)$. We investigated several sets of reasonable criteria for dimers based on r and θ. All of the sets tested gave qualitatively similar results, revealing a population of neighboring head-to-tail dimers, with many molecules forming dimers with more than one neighbor. In Fig. S3A we show a comparison of the populations of dimers for the different sets of criteria. Here we use the criteria 3.5 Å $\leq r_{\text{Me-CN}} \leq$ 4.2 Å and $0^\circ \leq \theta \leq 90^\circ$. We isolated molecular pairs meeting these criteria and calculated the angle α formed by the unit vector along the principal molecular axis of a molecule 1 with the unit vector between the methyl group of a molecule 1 and the cyano group of a molecule 2, as indicated schematically in Fig. 5. We used this information to assess whether head-to-tail pairing predominantly involves end-on or offset associations. Fig. 5 shows the probability that two acetonitrile molecules that meet the above criteria are separated by a distance r and make an angle α. Note that we have normalized the data to $P(r)$, the probability of the molecules in the pair having a center-of-mass separation of r for each r. The probability $P'(\alpha)$ of the molecules in the pair having an angle α is also shown. For end-on dimers, we would expect the latter distribution to be peaked at a relatively small value of α, with the center-of-mass separation decreasing with increasing α. The fact that the peak occurs at an angle of ~97° indicates, however, that offset head-to-tail dimers dominate this population. This picture is confirmed by the representative pair configuration shown (configuration 12). The appearance of molecular pairs at angles greater than

90˚ (configurations 12 and 13) is a clear sign that offset pairing is dominant. An end-on configuration is also shown (configuration 14) for comparison.

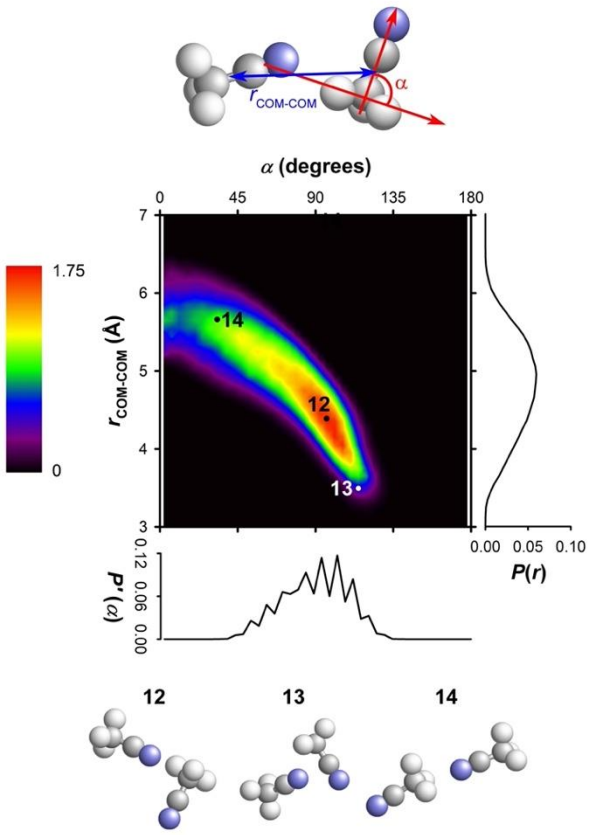

Fig. 5 Analysis of head-to-tail dimers, with the angle α defined by the unit vector along the principal molecular axis of a molecule 1 with the unit vector between the methyl group of the molecule 1 and the cyano group of a molecule 2. The directions of the unit vectors are illustrated schematically in the figure. The probabilities $P(r)$ and $P'(\alpha)$ are defined as described in the text.

Together, these results point to the existence of two distinct pair populations in liquid acetonitrile: antiparallel, octupole-paired molecules, and offset, head-to-tail molecules. It is interesting to explore whether these same motifs are prominent in the common crystalline phases of acetonitrile. We therefore determined the angularly resolved radial distribution functions for the α and β crystalline polymorphs of acetonitrile, based on crystallographic data [100]. The $g(r,\theta)$ for the Me-CN and CN-CN interactions for both phases are shown in Fig. 6. For the high-temperature α

polymorph, $g_{\text{Me-CN}}(r,\theta)$ reveals the presence of a substantial population of perpendicular, end-on, head-to-tail dimers (configuration 15) and parallel, offset dimers (configuration 16) that are not common in the liquid. There are also dimers that are arranged in an octupole-paired fashion (configuration 17) that correspond strongly with the liquid structure. The corresponding $g_{\text{Me-CN}}(r,\theta)$ for the β polymorph features perpendicular, offset, head-to-tail dimers (configuration 18) that have a strong presence in the liquid. However, the highest peak in this angularly-resolved radial distribution function is for parallel head-to-tail dimers that do not feature prominently in the liquid (configuration 19), in addition to roughly perpendicular, offset, head-to-tail dimers (configuration 20), again as found in the liquid.

The plot of $g_{\text{CN-CN}}(r,\theta)$ for the α polymorph in Fig. 6 reveals populations of octupole-paired dimers (configuration 21), and perpendicular, offset, head-to-tail dimers (configuration 22), as in the bulk liquid. There are also offset parallel dimers (configuration 23) that are not present in the bulk liquid. In the β polymorph, the largest peak arises from offset parallel dimers (configuration 24) that do not have a strong presence in the liquid. There is a peak corresponding to roughly perpendicular head-to-tail dimers (configurations 25) that is important in the liquid, in addition to another strong peak corresponding to offset parallel dimers (configuration 26). The angularly resolved radial distribution functions for the center-of-mass and Me-Me separations tell a similar story (Fig. S4). We can conclude that the offset parallel dimers that are seen in the crystalline phase are driven by packing constraints, whereas the offset, head-to-tail and octupole-paired dimers present in all three phases are energetically favorable.

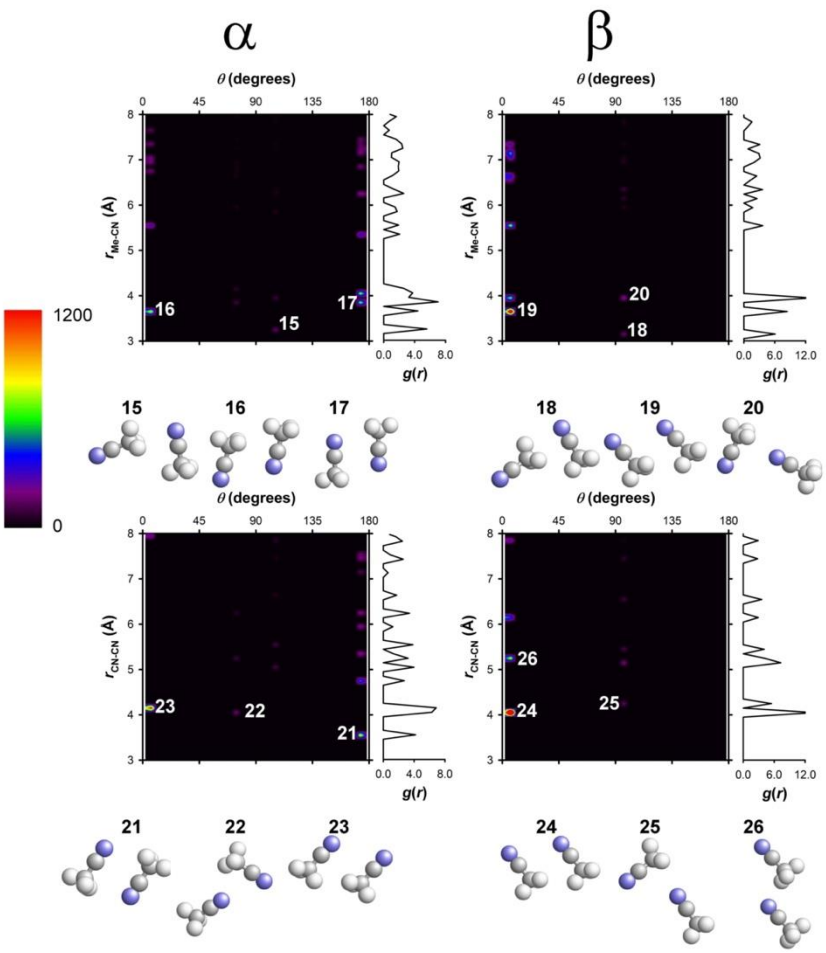

Fig. 6 Radial distribution functions and angularly resolved radial distribution functions for crystalline acetonitrile with respect to the methyl-cyano distance for the α polymorph (top left) and the β polymorph (top right) as well as with respect to the cyano-cyano distance for the α polymorph (bottom left) and for the β polymorph (bottom right).

To examine the forces behind octupole pairing of our model in more detail, we calculated the gas-phase multipole moments through the octupole moment (Table 1). For our calculations, the reference frame was centered about the molecular center of mass, with the *z* axis pointing toward the methyl group. Although some of the tensor elements for the higher moments of ACN are non-negligible, the value for the octupole moment is considerably less than the calculated values for fluoroacetylene [105,106], which we use as a benchmark molecule due to its linear geometry and the alternating signs of its charges. The small magnitude of the octupole moment suggests that electrostatic forces are not the driving force for the pairing that we observe. It is important to note,

however, that the contribution of different non-vanishing multipole moments to the properties of molecular liquids is not yet well understood [107], and the octupole moment of ACN has been shown to be important for the solvation of ions [18] and to contribute to the dielectric constant [108].

Table 1 Multipole moments for acetonitrile and comparison to other molecules.

Moment	ACN (literature or **this work**)	Comparison
μ_z (D)	3.92[a], **4.02**	1.855[b] (H_2O)
Θ_{zz} (DÅ)	-1.8[c], -2.28[d], -2.55[e], **-2.50**	-8.69[f] (C_6H_6)
Ω_{zzz} (DÅ^2)	**5.47**	16.9[g], 20.2[h] (HC_2F)
Ω_{xxx} (DÅ^2)	**1.84**	

[a-c,f] Experiment (Refs. [1], [101], [102], and [103], respectively). [d,e,g,h] Computation (Refs. [104], [16], [105], and [106], respectively).

To delve further into the driving force for the pairing in liquid acetonitrile, we calculated the average Coulomb energy per pair based on r and θ for the centers of mass, for Me and CN, and for CN and CN. The resultant plots are shown in Fig. S5, and indicate that pairs with CN dipole pairing (i.e, with r less than ~3.3 Å and θ near 180°) have the most favorable Coulombic interactions, although the Me-CN interactions that correspond to octupole-paired molecules are nearly as strong. However, it is clear from Fig. 4 that the population of dipole-paired molecules is small, and the plots in Fig. S5 do not account for the prevalence of pairs at specific r and θ. We therefore multiplied each distribution by the corresponding $g(r,\theta)$. The resultant plots are shown in Fig. 7, and emphasize regions in which there is a high probability of having pairs, and where the pair Coulombic energy has a large magnitude. The contribution of dipole-paired molecules to the CN-CN plot is vanishingly small, and all three plots are consistent with octupole-paired molecules making the greatest contribution to the average pair Coulomb energy.

Earlier works that stressed the importance of dipole-dipole interactions on the structure of liquid ACN were not able to reproduce real-space representations of the structure when the charges were turned off [13,23,33]. However, given that all Coulomb interactions between pairs that we have found are considerably smaller than the thermal energy, electrostatic forces cannot be the major driving force in determining the preferred pair structures. It is clear from our results as well that

pairwise electrostatic interactions are not primarily responsible for the preference of octupole-paired dimers over dipole-paired dimers. This preference must instead be a result of collective effects, such as packing constraints. Our results are therefore consistent with the work of Hsu and Chandler, who attributed the organization in acetonitrile largely to the molecular shape, rather than to electrostatic interactions [11].

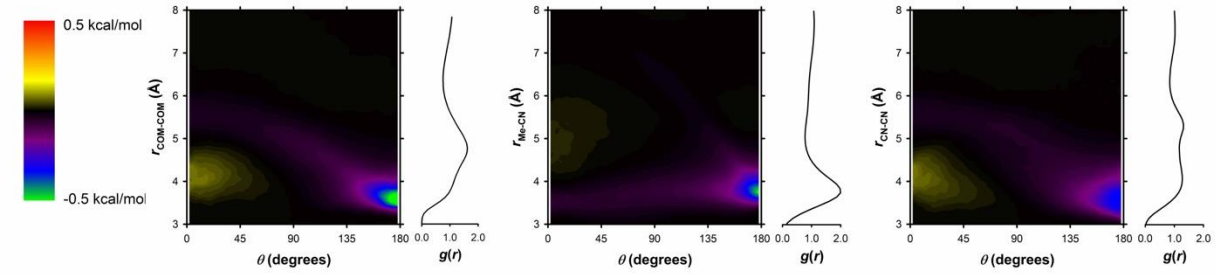

Fig. 7 Pair Coulomb energies weighted by $g(r,\theta)$ and radial distribution functions for acetonitrile with respect to the center-of-mass distance, methyl-cyano distance, and cyano-cyano distance. Pair Coulomb energies were calculated in kcal/mol, and the bin size is 0.1 Å in r and 5° in θ.

To analyze the pairing in the liquid in more detail, we created a 2D histogram of the number of paired antiparallel and head-to-tail molecules (Fig. 8), with the pairing for antiparallel molecules defined, based on $g_{CN\text{-}CN}(r,\theta)$, by the criteria 3.1 Å ≤ $r_{CN\text{-}CN}$ ≤ 4.6 Å and 135° ≤ θ ≤ 180° (for a comparison of different criteria, see Fig. S3B). The 1D probabilities $P(n)$ for either antiparallel or head-to-tail dimers are given alongside the 2D histogram. It is clear from Fig. 8 that molecules are not necessarily paired only to a single neighbor, and that molecules participating in head-to-tail

pairs are rarely paired only to one neighbor. It is noteworthy that fewer than 2% of molecules are unpaired at any given time. The lifetimes of pairs are discussed below in Sec. 3.2.1.

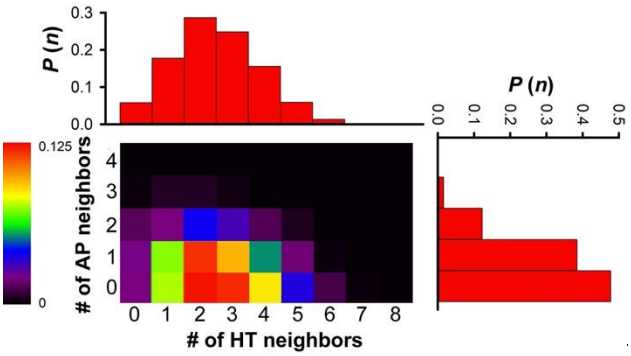

Fig. 8 Probability that an acetonitrile molecule is associated with antiparallel (AP) or head-to-tail (HT) neighbors, as defined in the text.

3.2. Dynamics and Vibrational Properties

3.2.1. Molecular Dynamics

Fig. 9 shows the mean-squared displacement (MSD) as a function of time for each atomic site, as determined from the molecular dynamics trajectory. As expected, in the long-time limit, all of the atomic MSDs overlap, because rotations and individual motions become negligible compared to the typical center-of-mass displacements. In this long-time limit, the self-diffusivity can be obtained from atomic MSDs using the Einstein equation, $D_s \sim \Delta r^2/6t$ [92]. From the MSDs, we calculated a value of 3.79×10^{-5} cm^2/s for the self-diffusion coefficient (Table 2). This self-diffusivity is somewhat lower than the experimental value, in agreement with previous results for this force field [76]. Additional useful dynamic information can be inferred from the short-time behavior of the atomic MSDs in Fig. 9. The hydrogen atoms, which are light, are in a superdiffusive, ballistic regime at short times, due to the spinning of the molecule about its long axis (methyl rotation). Because spinning constrains the hydrogen atoms to move in circles, the hydrogen-atom MSD only appears ballistic on sufficiently short time scales. The fact that the hydrogen atoms are farther from the molecular center of mass than are any other atoms means that tumbling rotation makes this MSD larger than any of the other atomic MSDs until such time as the Fickian limit is reached. Conversely, the central carbon (YC) is close to the center of mass,

which means that its MSD is the least affected by tumbling, and is slightly smaller than the values for the other atomic sites until the Fickian limit is reached.

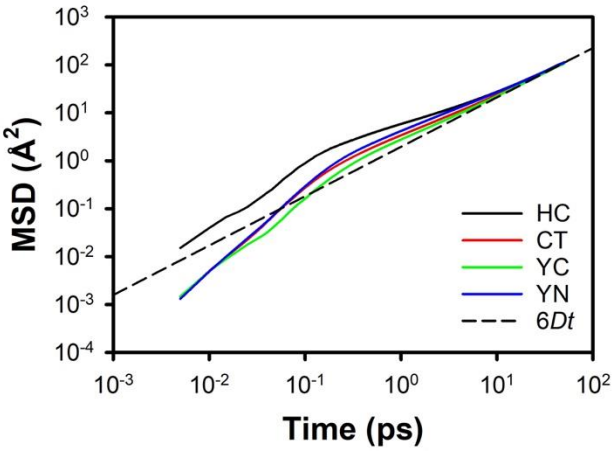

Fig. 9 Mean-squared displacement as a function of time for each atomic site. The dashed line indicates the Fickian limit, in which the MSD is given by 6*Dt*.

Table 2 Self-diffusivity for acetonitrile and acetonitrile-d_3, along with a comparison to values from the literature.

Property	Simulation (this work)	Experiment (literature or **this work**)
Self-diffusivity (10^{-5} cm^2/s)	3.79[a]	4.12[b], 4.2[c], 4.3[d], 4.31[e], 4.34[f], 4.37[g,h], 4.7[i], 5.0[j], **4.24**
Self-diffusivity, ACN-d_3 (10^{-5} cm^2/s)	3.64[a]	4.04[j], 4.14[l], **3.94**

[a] Calculated via mean-squared displacement. [b] Determined in Ref. [109] from conductivity measurements. [c] Determined in Ref. [44] from quasielastic neutron scattering measurements. [d,e] Determined, respectively, in Refs. [110] and [111] from NMR spin echo measurements. [f] Determined in Ref. [112] via an open-ended capillary method. [g-l] Determined, respectively, in Refs. [113], [114], [45], [6], [115], and [113] from NMR spin-echo measurements.

The simulated vibrational density of states $g(\omega)$ was calculated for each atom, and for the center of mass, using

$$g(\omega) = \frac{1}{2\pi}\mathrm{Re}\left[\mathrm{FT}\left(C(\tau)\right)\right] \ , \tag{20}$$

where $C(\tau) = \langle v(0) \cdot v(\tau) \rangle$ is the velocity autocorrelation function. These velocity autocorrelation functions are plotted in Fig. S6. For the calculation of the simulated vibrational

density of states, only the first half of the velocity autocorrelation function was used, and the autocorrelation function was padded with zeros out to ~65 ps. A Savitzky-Golay filter was used to smooth the data. The GDOS was obtained by weighting the vibrational densities of states for each atomic site according to Eq. (7), using the neutron incoherent scattering cross sections. The low-frequency GDOS is shown in Fig. 10A. This region of the spectrum corresponds to intermolecular modes. The partial densities of states for each site and for the center of mass are shown in Fig. 10B. In the case of the center-of-mass vibrational density of states, the low-frequency region reflects the influence of molecular tumbling, and thus can be regarded, in a sense, as a single-molecule analog to the low-frequency Raman spectrum. In Fig. 10A, we also show the density of states as obtained from inelastic neutron scattering; these data are discussed in detail below in Section 3.2.2. In the simulated data, modes due to the intramolecular part of the force field appear at higher frequencies, as shown in Fig. 10B. Table 3 lists the modes and their assignments. We also performed a normal-mode analysis along the molecular axis, using previously reported force constants [76] and a unified methyl group.

Table 3 Type of intramolecular mode and corresponding experimental frequency. The approximate frequencies of the modes in the model are also given.

Mode	**Experiment[a] (cm^{-1})**	**Simulation (cm^{-1})**	**Degeneracy**
CCN bend	379	631	2
CC stretch	917	832	1
CH_3 rock	1040	956	2
CH bend	1372	1318	1
CH bend	1440	1388	2
CN stretch	2253	1722	1
CH stretch	2943	2921	1
CH stretch	3003	3036	2

[a] Ref. [42].

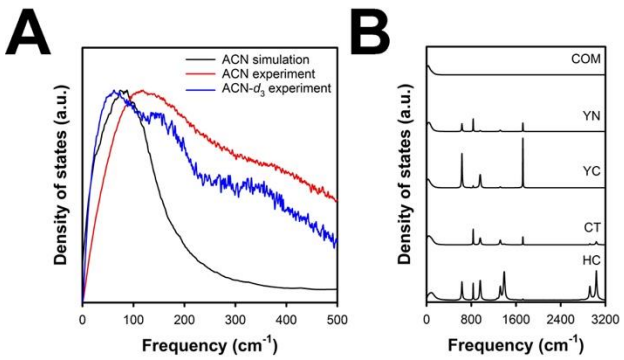

Fig. 10 (A) Low-frequency region of the simulated generalized density of states for ACN, along with an overlay of the experimental, height-normalized inelastic neutron spectra for ACN and ACN-d_3. (B) Full spectra of the simulated vibrational density of states for ACN calculated with respect to the molecule center of mass (COM, top spectrum) and for each atomic site on the molecule. The densities of states are offset vertically for clarity.

We investigated the pairing lifetime for both the antiparallel and head-to-tail configurations, as defined in Section 3.1.1. We employed the formalism of Impey *et al.* [116], in which the mean first passage time [117] is used to calculate $\Psi(t)dt$, the probability that a molecule that is paired at time $t = 0$ remains paired at a time t [118,119]. As proposed by Impey *et al.* [116], we introduce a tolerance time, τ^*, over which two molecules are allowed to be unpaired. In other words, if the molecules unpair for a time shorter than τ^* but are paired both before and after, then these molecules are still considered as having remained paired. $\Psi(t,\tau^*)\,dt$ is the probability that a molecule remains continuously paired to any molecule at a time t after being paired at a time $t = 0$. As discussed by Laage and Hynes [120], transition-state theory is a more robust tool for determining pairing times, as the approach used here is τ^*-dependent. The τ^* approach is, however, sufficient to investigate the phenomena in which we are interested, particularly because our neutron-scattering experiments have a time resolution of ~1 ps. Thus, $\tau^* = 1$ ps is ideal for comparison of our simulations with our experimental data.

Fig. 11 shows $\Psi(t,\tau^*)$ for both antiparallel and head-to-tail configurations for different τ^*. It is clear that the typical antiparallel pairing time is shorter than the head-to-tail pairing time. This observation is consistent with the histogram in Fig. 8, which indicates that the population of head-

to-tail pairs is larger than that of antiparallel pairs. A molecule in a head-to-tail pair has a longer pairing lifetime because it has many nearest neighbors with which it may pair in this configuration. As τ^* increases, we find that the majority of molecules that participate in head-to-tail pairs remain paired almost continuously. In contrast, for molecules participating in antiparallel pairs, even when the value of τ^* is large, the pair lifetime is considerably shorter than that for head-to-tail pairs.

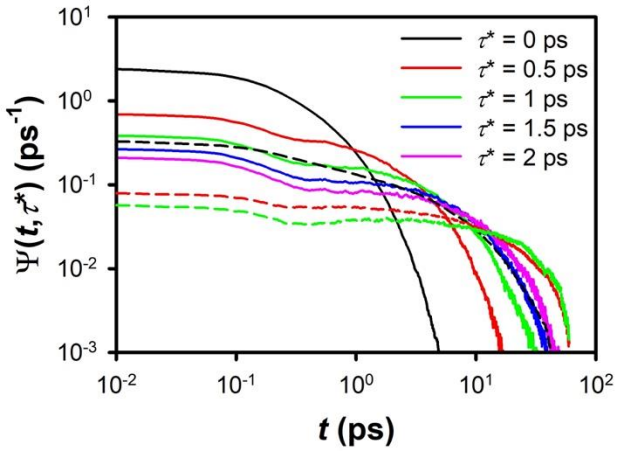

Fig. 11 Mean first passage times for molecules in pairs, calculated following the methodology of Impey *et al* [116]. The solid lines correspond to antiparallel pairs and the dashed lines correspond to head-to-tail pairs. The curves are color-coded by the tolerance time τ^*; note that results are only shown for head-to-tail pairs out to τ^* = 1 ps.

3.2.2. Neutron scattering

Neutron-scattering data for ACN and ACN-d_3 provide complementary information, due to the different neutron-scattering cross sections of hydrogen and deuterium. In particular, because of the large incoherent cross section of hydrogen, the spectrum of ACN is dominated by information on the individual dynamics of hydrogen, i.e., the methyl group.

Neutron GDOS. The generalized densities of states extracted from neutron scattering measurements are shown in Fig. 12A. The most striking feature is the intensity and width of the low-frequency region, extending up to 500 cm^{-1}. We assign this feature in the experimental neutron

density of states to the intense scattering from the methyl group, which arises from librational motion and is broadened by multiphonon contributions, and is ultimately convolved with the translational dynamics. For the deuterated sample, the intensity between 150 and 300 cm^{-1} also suffers from imperfect subtraction of the empty cell in this region (DOS of aluminum, see Fig. S7). The small bump at 390 cm^{-1} in the ACN-d_3 spectrum corresponds to the IR- and Raman-active CCN bending mode [42], which does not have a strong intensity in inelastic neutron scattering.

QENS. The quasielastic signal gives insight into diffusional dynamics. Simulated dynamical structure factors $S(q,\omega)$ were obtained by Fourier transforms of the intermediate coherent scattering functions $F_{coh}(q,t)$ [121]. As shown in Fig. 12, the spectra at different q values are well reproduced by our simulations. Our first analysis of the experimental data was based on a model composed of two Lorentzian contributions, without making any specific hypothesis regarding the diffusive dynamics. The widths of the two contributions for ACN and ACN-d_3 are shown in Fig. 13. Fig. 13A shows a clear translational contribution, with the width depending linearly on q^2, whereas Fig. 13B shows broad contributions with a mixed localized and translational character. Both types of dynamics in ACN-d_3 are slowed down at momentum values approaching the maximum of the structure factor, which is a typical effect observed in coherent neutron scatterers that is described as de Gennes narrowing [122]. A more refined model was therefore proposed based on two isotropic rotational contributions, convolved by the same translational dynamics, and modeled by a jump-diffusion behavior. We constrained the rotational radii to 1.03 and 1.9 Å, corresponding, respectively, to the spinning and tumbling of the molecule. The de Gennes narrowing was taken into account by constraining D_T of the deuterated compound to follow the modulation of the structure factor, according to the relation

$$\Gamma_T = \frac{D_T q^2}{1+\tau D_T q^2}\frac{1}{S(q)} \quad . \tag{21}$$

Using this framework, we were able to extract the translational and rotational diffusion coefficients, residence times τ_{res}, and spinning and tumbling times τ_{spin} and τ_{tumbling}, respectively (Table 4). The spinning mode has a short characteristic time (~0.2-0.3 ps), which is in agreement with previous QENS [44] and NMR [123] studies. The tumbling mode has a longer characteristic time (1.6-2 ps), which also is in agreement with previous spectroscopic work [44]. We also fitted the simulated $S(q,\omega)$ with the same model. Constraining the translational diffusion coefficient to

3.79×10^{-5} cm^2/s, as extracted from the MSDs, and the rotational radii as 1.03 Å and 1.9 Å from the experimental data, we find rotational constants of 1.79 ± 0.07 and 0.26 ± 0.02 ps^{-1} for the tumbling and spinning motions, respectively, which is in excellent agreement with the values extracted from the experimental spectra.

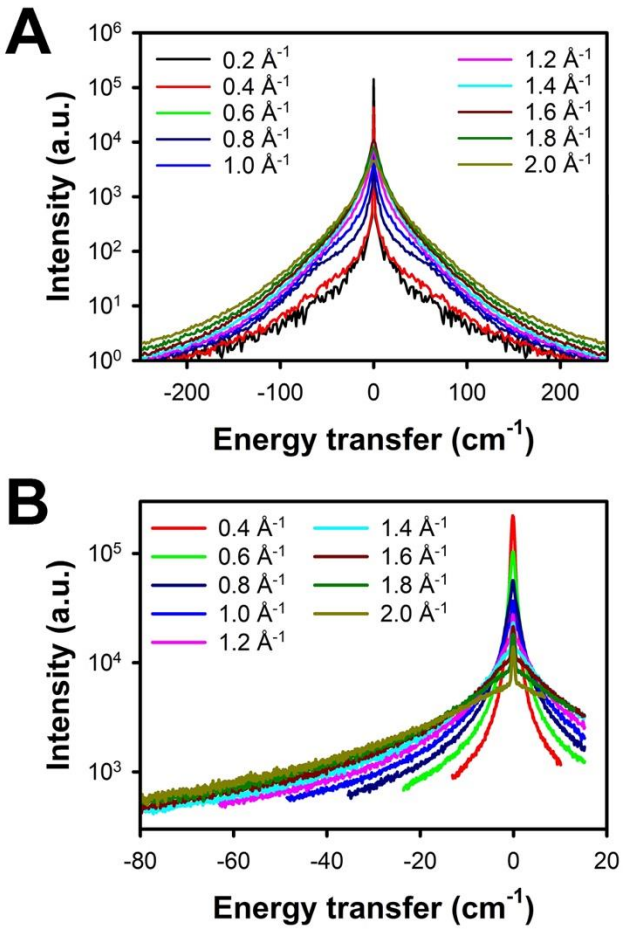

Fig. 12 $S(q,\omega)$ as a function of energy transfer ω for ACN obtained from (A) molecular dynamics simulations and (B) quasielastic neutron scattering. The legends indicate the different values of q that were used. The quasielastic neutron scattering experiments were performed with an incident energy E_i = 2.83 meV.

Table 4. Translational diffusion coefficients D_T, rotational diffusion coefficients for tumbling $D_{rot,tumbling}$ and spinning $D_{rot,spin}$, along with residence times τ_{res}, and spinning and tumbling times τ_{spin} and $\tau_{tumbling}$, respectively, for both acetonitrile and acetonitrile-d_3.

Species	D_T **(10^{-5} cm^2/s)**	$D_{rot,tumbling}$ **(ps^{-1})**	$D_{rot,spin}$ **(ps^{-1})**	τ_{res} **(ps)**	$\tau_{tumbling}$ **(ps)**	τ_{spin} **(ps)**
ACN	4.24 ± 0.3	0.26 ± 0.03	1.77 ± 0.1	0.42 ± 0.1	1.94 ± 0.02	0.29 ± 0.02
ACN-d_3	3.94 ± 0.4	0.3 ± 0.03	1.91 ± 0.15	0.42 ± 0.1	1.66 ± 0.01	0.26 ± 0.02

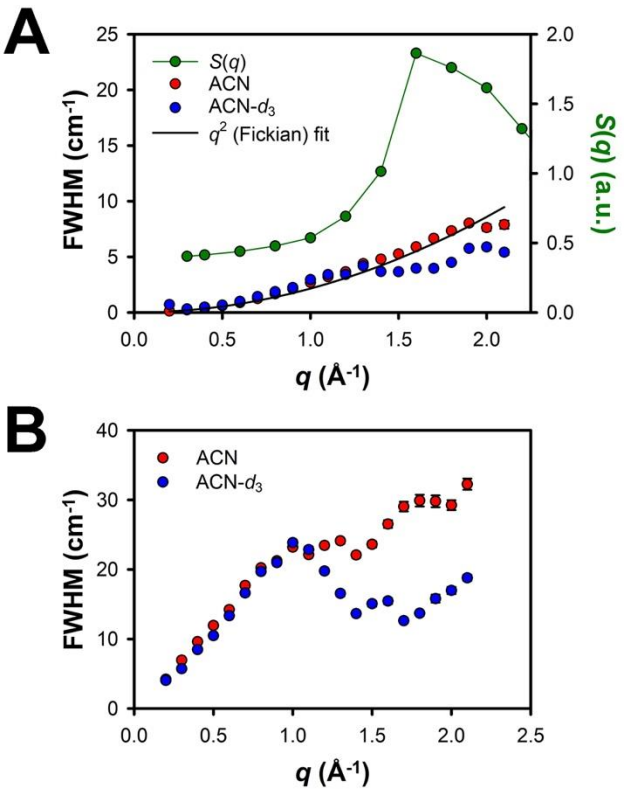

Fig. 13 (A) The QENS data from Fig. 12B were analyzed with a sum of two Lorentzian contributions whose full-widths at half maximum (FWHMs) are shown on panels (A) and (B). (A) FWHM of the translational contribution, with the values for D_s(ACN) and D_s(ACN-d_3) as in Table 2. The data for ACN-d_3 exhibit de Gennes narrowing at q ~ 1.6 Å^{-1}, which is at the maximum of the structure factor $S(q)$ (also shown for comparison). The fit is to the data for ACN. (B) The larger contribution is characteristic of a fast transition fitted with a jump-diffusion model, and is assigned to the coupling between translation and the rotation of the methyl groups.

4. Discussion and Conclusions

We have presented a detailed investigation of the structure and dynamics of bulk liquid ACN based on a combination of molecular simulation and neutron-scattering experiments. Our structural results obtained using molecular simulations reveal a complex organization in which molecules tend to form oriented dimers with their neighbors. Such marked pairing, which leads to characteristic pairing times that extend beyond the typical rotational and translational times, results from collective interactions. Although the classic picture of pairing in ACN involves the antiparallel organization of neighboring cyano groups via dipole pairing, we find that the antiparallel organization is best described in Coulombic terms as octupole pairing, although the driving interaction for such pairing is collective rather than electrostatic. Furthermore, head-to-tail pairing is an even more prevalent and robust motif. However, as discussed above, this head-to-tail pairing does not predominantly involve end-on interactions. Rather, the nitrogen atom of one molecule has a propensity to interact with the hydrogen atoms on the side of the methyl group of another molecule.

These results suggest that the microscopic organization of ACN is determined by a complex interplay among different structural motifs. ACN dimers in vacuum and in helium droplets are known to take on an antiparallel structure [124]. Free trimers are believed to be "liquid-like," whereas in helium droplets the preferred trimer structure consists of a dimer with an associated monomer [124]. The free tetramer has a structure composed of two perpendicular dimers (S_4 symmetry), whereas in a helium droplet the molecules form a ring with alternating dipole pairing (D_{2d} symmetry) [124]. In contrast, the common crystalline phases of acetonitrile are characterized by head-to-tail interactions, as opposed to antiparallel interactions [100], as shown above. As in our simulations, the head-to-tail interactions are predominantly offset, rather than end-on. The strong contrast between the crystal structure and the cluster structure may reflect packing constraints, e.g., the inability to create a stable, 3D, space-filling structure whose main motif is octupole pairing. A liquid is three-dimensional, but does not fill space in a regular pattern. From this perspective, it is perhaps not surprising that our simulations indicate that the liquid has elements of both the cluster and crystalline structure. We do observe a significant population of dipole-paired dimers and trimers, but head-to-tail structures are considerably more prevalent.

Our pairing analysis of the antiparallel and head-to-tail motifs found in the bulk liquid shows that nearly all of the molecules are paired at any given time, and most molecules are paired to more than one neighbor. Additionally, the antiparallel pairing lifetime, as defined using the formalism of mean first passage time while allowing for a short escape time in pairing, is shorter than the head-to-tail pairing lifetime. This finding, which is not unique to a particular choice of initial conditions, is consistent with the fact there are more head-to-tail paired molecules than antiparallel paired molecules. Our results can be understood based on the idea that head-to-tail dimers, unlike antiparallel dimers, do not experience any strong directional forces. The prominence of head-to-tail dimers is presumably an entropic effect, which further suggests that this feature is not unique to the force field used here.

Our findings highlight the ability of angularly-resolved radial distribution functions to provide a wealth of information about the organization of bulk liquid acetonitrile. Although this methodology has been used previously to study microheterogeneities in simulations of ACN/water mixtures [61], the angularly-resolved radial distribution functions in that work were not calculated with respect to the functional groups of ACN; as demonstrated here, doing so yields important new insights. In studies of liquid ACN at silica interfaces, applying the pairing analysis may also be helpful in teasing out details of the lipid-bilayer-like organization that forms in such systems [49]. In particular, using angularly-resolved radial distribution functions and pairing analysis to study the population of tail-to-tail dimers at the silica interface is expected to reveal key details about the ACN bilayer.

CRediT Authorshiop Contribution Statement. Samuel R. Cohen: Formal Analysis, Investigation, Visualization, Writing – Original Draft. **Marie Plazanet:** Formal Analysis, Investigation, Methodology, Writing – Original Draft. **Stéphane Rols:** Writing – Review & Editing. **David J. Voneshen:** Data Curation, Writing – Review & Editing. **John T. Fourkas:** Conceptualization, Formal Analysis, Funding Acquisition, Project Administration, Supervision, Visualization, Writing – Review & Editing. **Benoit Coasne:** Conceptualization, Formal Analysis, Investigation, Supervision, Writing – Original Draft.

Declaration of Competing Interest. We have no conflicts of interest to declare.

Acknowledgments. This material is based upon research supported by the Chateaubriand Fellowship of the Office for Science & Technology of the Embassy of France in the United States and by the National Science Foundation, grant CHE-1800491. Some of the computations presented in this paper were performed using the Froggy platform of the GRICAD infrastructure (https://gricad.univ-grenoble-alpes.fr), which is supported by the Rhône-Alpes region (GRANT CPER07_13 CIRA) and the Equip@Meso project (reference ANR-10-EQPX-29-01) of the programme Investissements d'Avenir supervised by the Agence Nationale pour la Recherche. We thank Dr. John Bender for helpful discussions and for results that motivated the work reported here, and Dr. Alexei Nikitin, Prof. Alexander Lyubartsev, and Dr. Szilvia Pothoczki for helpful correspondence.

5. References

1. Steiner, P. A.; Gordy, W. Precision Measurement of Dipole Moments and Other Spectral Constants of Normal and Deuterated Methyl Fluoride and Methyl Cyanide. *J. Mol. Spectrosc.* **1966**, *21*, 291−301.
2. McConvey, I. F.; Woods, D.; Lewis, M.; Gan, Q.; Nancarrow, P. The Importance of Acetonitrile in the Pharmaceutical Industry and Opportunities for its Recovery from Waste. *Org. Process Res. Dev.* **2012**, *16*, 612−624.
3. Yamada, Y.; Furukawa, K.; Sodeyama, K.; Kikuchi, K.; Yaegashi, M.; Tateyama, Y.; Yamada, A. Unusual Stability of Acetonitrile-Based Superconcentrated Electrolytes for Fast-Charging Lithium-Ion Batteries. *J. Am. Chem. Soc.* **2014**, *136*, 5039−5046.
4. Saitô, H.; Tanaka, Y.; Nagata, S.; Nukada, K. ^{13}C Nuclear Magnetic Resonance Studies on Molecular Association. I. Self-Association of Dipolar Molecules. *Can. J. Chem.* **1973**, *51*, 2118−2123.
5. Kratochwill, A.; Weidner, J. U.; Zimmermann, H., Röntgenstrukturuntersuchung des flüssigen Acetonitrils. *Ber. Bunsenges. Phys. Chem.* **1973,** *77*, 408−425.
6. Kratochwill, A. ^{13}C-^{1}H Intermolecular Relaxation Rate and Molecular Pair Distribution Function in Liquid Acetonitrile. *Ber. Bunsenges. Phys. Chem.* **1978**, *82*, 783−789.
7. Versmold, H. Depolarized Rayleigh Scattering: Reorientational Motion and Orientational Correlation in Acetonitrile and Carbon Disulfide. *Ber. Bunsenges. Phys. Chem.* **1978**, *82*,

451−457.

8. Bertagnolli, H.; Chieux, P.; Zeidler, M. D. A Neutron-Diffraction Study of Liquid Acetonitrile: I. $CD_3C^{14}N$. *Mol. Phys.* **1976**, *32*, 759−773.
9. Bertagnolli, H.; Chieux, P.; Zeidler, M. D. A Neutron-Diffraction Study of Liquid Acetonitrile: II. $CD_3C^{15}N$. *Mol. Phys.* **1976**, *32*, 1731−1736.
10. Bertagnolli, H.; Zeidler, M. D. Molecular Pair-Correlation Function of Liquid Acetonitrile from X-Ray and Neutron-Diffraction Studies. *Mol. Phys.* **1978**, *35*, 177−192.
11. Hsu, C. S.; Chandler, D. RISM Calculation of the Structure of Liquid Acetonitrile. *Mol. Phys.* **1978**, *36*, 215−224.
12. Fraser, K. J.; Morriss, G. P.; Dunn, L. A. On the Structure Factor of Dipolar Molecular Fluids. *Mol. Phys.* **1986**, *57*, 1233–1245.
13. Fraser, K. J.; Dunn, L. A.; Morriss, G. P. An Integral Equation Study of Liquid Acetonitrile. *Mol. Phys.* **1987**, *61*, 775–782.
14. Steinhauser, O.; Bertagnolli, H. Molecular Pair Correlation Function of Liquid Acetonitrile Derived from Perturbation Theory with a Computer-Generated Reference Function. *Chem. Phys. Lett.* **1981**, *78*, 555–559.
15. Salamito, B.; Fries, P. H. Structure Factor Calculations for Molecular Liquids: Beyond the RISM Approximation. *Physica B* **1989**, *156–157*, 161–163.
16. Fries, P. H.; Richardi, J.; Krienke, H. Dielectric and Structural Results for Liquid Acetonitrile, Acetone and Chloroform from the Hypernetted Chain Molecular Integral Equation, *Mol. Phys.* **1997**, *90*, 841–854.
17. Richardi, J.; Fries, P. H.; Fischer, R.; Rast, S.; Krienke, H. J. Structure and Thermodynamics of Liquid Acetonitrile via Monte Carlo simulation and Ornstein-Zernike theories. *J. Mol. Liq.* **1997**, *73–74*, 465–485.
18. Fries, P. H.; Kunz, W.; Calmettes, P.; Turq, P. Molecular Solvent Model for a Cyprate Solution in Acetonitrile: A Hypernetted Chain Study. *J. Chem. Phys.* **1994**, *101*, 554–577.
19. Fries, P. H.; Kunz, W.; Calmettes, P.; Turq, P. Pictorial Intuition of the Correlation between Structure and Properties in Liquid Solutions: Acetonitrile as a Strongly Structured Solvent of Dissociated Ions. *J. Mol. Struct.* **1995**, *330*, 287–300.
20. Böhm, J. B.; Lynden-Bell, R. M.; Madden, P. A.; McDonald, I. R. Molecular Motion in a

Model of Liquid Acetonitrile. *Mol. Phys.* **1984**, *51*, 761−777.

21. Westlund, P.-O.; Lynden-Bell, R. M. A Molecular Dynamics Study of the Intermolecular Spin-Spin Dipole-Dipole Correlation Function of Liquid Acetonitrile. *J. Magn. Reson.* **1987**, *72*, 522−531.
22. Kovacs, H.; Kowalewski, J.; Laaksonen, A. Molecular Dynamics Simulation of Liquid Mixtures of Acetonitrile and Chloroform, *J. Phys. Chem.* **1990**, *94*, 7378−7385.
23. Ohba, T.; Ikawa, S. Molecular Dynamics Study of Local Structure and Reorientational Dynamics in Liquid Acetonitrile. *Mol. Phys.* **1991**, *73*, 999−1010.
24. La Manna, G.; Notaro, C. E. Montecarlo Calculation of the Structure of Liquid Acetonitrile. *J. Mol. Liq.* **1992**, *54*, 125−130.
25. Radnai, T.; Jedlovszky, P. Reverse Monte Carlo Simulation of a Heteronuclear Molecular Liquid: Structural Study of Acetonitrile. *J. Phys. Chem.* **1994**, *98*, 5994−6002.
26. Terzis, A. F.; Samulski, E. T. Spatial Distribution Functions: Liquid CH_3CN and CO_2, *Chem. Phys. Lett.* **1996**, *251*, 157–163.
27. Mountain, R. D. Shear Viscosity and Dielectric Constant of Liquid Acetonitrile. *J. Chem. Phys.* **1997**, *107*, 3921−3923.
28. Hirata, Y. Molecular Dynamics Simulation Study of the Rotational and Translational Motions of Liquid Acetonitrile. *J. Phys. Chem. A* **2002**, *106*, 2187−2191.
29. Gerig, J. T. Simulations of Nuclear Spin Relaxation in Liquid Acetonitrile. *Mol. Simul.* **2012**, *38*, 1085−1093.
30. Pothoczki, S.; Pusztai, L. Intermolecular Orientations in Liquid Acetonitrile: New Insights Based on Diffraction Measurements and All-Atom Simulations. *J. Mol. Liq.* **2017**, *225*, 160−166.
31. Evans, M. Molecular Dynamics and Structure of Liquid Acetonitrile – A Review and Computer Simulation. *J. Mol. Liq.* **1983**, *25*, 149–175.
32. Koverga, V. A.; Korsun, O. M.; Kalugin, O. N.; Marekha, B. A.; Idrissi, A. A New Potential Model for Acetonitrile: Insight into the Local Structure Organization. *J. Mol. Liq.* **2017**, *233*, 251−261.
33. Jorgensen, W. L.; Briggs, J. M. Monte Carlo Simulations of Liquid Acetonitrile with a Three-Site Model. *Mol. Phys.* **1988**, *63*, 547−558.
34. Edwards, D. M. F.; Madden, P. A.; McDonald, I. R. A Computer Simulation Study of the

Dielectric Properties of a Model of Methyl Cyanide: I. The Rigid Dipole Case. *Mol. Phys.* **1984**, *51*, 1141−1161.

35. Böhm, J. B.; McDonald, I. R.; Madden, P. A. An Effective Pair Potential for Liquid Acetonitrile. *Mol. Phys.* **1983**, *49*, 347−360.
36. Gee, P. J.; van Gunsteren, W. F. Acetonitrile Revisited: A Molecular Dynamics Study of the Liquid Phase. *Mol. Phys.* **2006**, *104*, 477–483.
37. Langer, H.; Versmold, H. Depolarized Rayleigh Scattering: Orientational Correlation Functions of Acetonitrile and Carbon Disulfide. *Ber. Bunsenges. Phys. Chem.* **1979,** *83*, 510−517.
38. Hashimoto, S.; Ohba, T.; Ikawa, S-I. Infrared and Molecular Dynamics Study of Reorientational Relaxation of Liquid Acetonitrile. *Chem. Phys.* **1989**, *138*, 63−69.
39. Yuan, P.; Schwartz, M. Molecular Reorientation in Acetonitrile: A Comparison of Diffusion Coefficients from Raman Bandshapes and Nuclear Magnetic Resonance Relaxation Times. *J. Chem. Soc. Faraday Trans.* **1990**, *86*, 593−596.
40. McMorrow, D.; Lotshaw, W. T. Intermolecular Dynamics of Acetonitrile Probed with Femtosecond Fourier Transform Raman Spectroscopy. *J. Phys. Chem.* **1991**, *95*, 10395−10406.
41. Giorgini, M. G.; Morresi, A.; Mariani, L.; Cataliotti, R. S. Molecular Reorientation in Liquid Acetonitrile Studied by Depolarized Light Scattering Experiments. *J. Raman Spectrosc.* **1995**, *26*, 601–605.
42. Deàk, J. C.; Iwaki, L. K.; Dlott, D. D. Vibrational Energy Redistribution in Polyatomic Liquids: Ultrafast IR-Raman Spectroscopy of Acetonitrile. *J. Phys. Chem. A* **1998**, *102*, 8193−8201.
43. Loughnane, B. J.; Scodinu, A.; Farrer, R. A.; Fourkas, J. T. Exponential Intermolecular Dynamics in Optical Kerr Effect Spectroscopy of Small-Molecule Liquids. *J. Chem. Phys.* **1999**, *111*, 2686–2694.
44. Kunz, W.; Calmettes, P.; Bellissent-Funel, M.-C. Dynamics of Liquid Acetonitrile at High Frequencies. *J. Chem. Phys.* **1993**, *99*, 2079−2082.
45. Zeidler, M. D. A Comparative Study of Quasielastic Neutron Scattering and NMR Relaxation in Liquid Acetonitrile. *Ber. Bunsenges. Phys. Chem.* **1971**, *75*, 769−776.

46. Saum, A. M. Intermolecular Association in Organic Nitriles; the CN Dipole-pair Bond. *J. Polym. Sci.* **1960**, *42*, 57−66.
47. Hu, Z.; Weeks, J. D. Acetonitrile at Silica Surfaces and at Its Liquid-Vapor Interface: Structural Correlations and Collective Dynamics. *J. Phys. Chem. C* **2010**, *114*, 10202–10211.
48. Ding, F.; Hu, Z.; Zhong, Q.; Manfred, K.; Gattass, R. R.; Brindza, M. R.; Fourkas, J. T.; Walker, R. A.; Weeks, J. D. Interfacial Organization of Acetonitrile: Simulation and Experiment. *J. Phys. Chem. C* **2010**, *114*, 17651–17659.
49. Berne, B. J.; Fourkas, J. T.; Walker, R. A.; Weeks, J. D. Nitriles at Silica Interfaces Resemble Supported Lipid Bilayers. *Acc. Chem. Res.* **2016**, *49*, 1605–1613.
50. Loughnane, B. J.; Farrer, R. A.; Fourkas, J. T. Evidence for the Direct Observation of Molecular Exchange of a Liquid at the Solid/Liquid Interface. *J. Phys. Chem. B* **1998**, *102*, 5409–5412.
51. Loughnane, B. J.; Farrer, R. A.; Scodinu, A.; Fourkas, J. T. Dynamics of a Wetting Liquid in Nanopores: An Optical Kerr Effect Study of the Dynamics of Acetonitrile Confined in Sol-Gel Glasses. *J. Chem. Phys.* **1999**, *111*, 5116–5123.
52. Yamaguchi, T.; Yoshida, K.; Smirnov, P.; Takamuku, T.; Kittaka, S.; Takahara, S.; Kuroda, Y.; Bellissent-Funel, M.-C. Structure and Dynamic Properties of Liquids Confined in MCM-41 Mesopores. *Eur. Phys. J. Spec. Top.* **2007**, *141*, 19–27.
53. Cheng, L.; Morrone, J. A.; Berne, B. J. Structure and Dynamics of Acetonitrile Confined in a Silica Nanopore. *J. Phys. Chem. C* **2012**, *116*, 9582–9593.
54. Milischuk, A. A.; Ladanyi, M. Polarizability Anisotropy Relaxation in Nanoconfinement: Molecular Simulation Study of Acetonitrile in Silica Pores. *J. Phys. Chem. B* **2013**, *117*, 15729–15740.
55. Thompson, W. H. Structure, Dynamics, and Hydrogen Bonding of Acetonitrile in Nanoscale Silica Pores. *Mol. Simul.* **2015**, *41*, 788–794.
56. Kovacs, H.; Laaksonen, A. Molecular Dynamics Simulation and NMR Study of Water-Acetonitrile Mixtures. *J. Am. Chem. Soc.* **1991**, *113*, 5596–5605.
57. Matsumoto, M.; Tanaka, H.; Nakanishi, K. Acetonitrile Pair Formation in Aqueous Solution. *J. Chem. Phys.* **1993**, *99*, 6935–6940.

58. Bergman, D. L.; Laaksonen, A. Topological and Spatial Structure in the Liquid-Water-Acetonitrile Mixture. *Phys. Rev. E* **1998**, *58*, 4706–4715.
59. Takamuku, T.; Tabata, M.; Yamaguchi, A.; Nishimoto, J.; Kumamoto, M.; Wakita, H.; Yamaguchi, T. Liquid Structure of Acetonitrile-Water Mixtures by X-ray Diffraction and Infrared Spectroscopy. *J. Phys. Chem. B* **1998**, *102*, 8880–8888.
60. Mountain, R. D. Molecular Dynamics Study of Water-Acetonitrile Mixtures. *J. Phys. Chem. A* **1999**, *103*, 10744–10748.
61. Oldiges, C.; Wittler, K.; Tönsing, T.; Alijah, A. MD Calculated Structural Properties of Clusters in Liquid Acetonitrile/Water Mixtures with Various Contents of Acetonitrile. *J. Phys. Chem. A* **2002**, *106*, 7147−7154.
62. Mountain, R. D. Microstructure and Hydrogen Bonding in Water-Acetonitrile Mixtures. *J. Phys. Chem. B* **2010**, *114*, 16460–16464.
63. Huang, N.; Nordlund, D.; Huang, C.; Bergmann, U.; Weiss, T. M.; Pettersson, L. G. M.; Nilsson, A. X-ray Raman Scattering Provides Evidence for Interfacial Acetonitrile-Water Dipole Interactions in Aqueous Solutions. *J. Chem. Phys.* **2011**, *135*, 164509.
64. Nagasaka, M.; Yuzawa, H.; Kosugi, N. Microheterogeneity in Aqueous Acetonitrile Solution Probed by Soft X-ray Absorption Spectroscopy. *J. Phys. Chem. B* **2020**, *124*, 1259–1265.
65. Roy, D.; Kovalenko, A. Application of the Approximate 3D-Reference Interaction Site Model (RISM) Molecular Solvation Theory to Acetonitrile as a Solvent. *J. Phys. Chem B* **2020**, *124*, 4590–4597.
66. Melnikov, S. M.; Höltzel, A.; Seidel-Morgenstern, A.; Tallarek, U. Composition, Structure, and Mobility of Water-Acetonitrile Mixtures in a Silica Nanopore Studied by Molecular Dynamics Simulations. *Anal. Chem.* **2011**, *83*, 2569–2575.
67. Mountain, R. D. Molecular Dynamics Simulation of Water-Acetonitrile Mixtures in a Silica Slit. *J. Phys. Chem. C* **2013**, *117*, 3923–3929.
68. Melnikov, S. M.; Höltzel, A.; Seidel-Morgenstern, A.; Tallarek, U. Adsorption of Water-Acetonitrile Mixtures to Model Silica Surfaces. *J. Phys. Chem. C* **2013**, *117*, 6620–6631.
69. Rivera, C. A.; Bender, J. S.; Manfred, K.; Fourkas, J. T. Persistence of Acetonitrile Bilayers at the Interface of Acetonitrile/Water Mixtures with Silica. *J. Phys. Chem. A* **2013**, *117*, 12060–12066.

70. Wang, Y.-P.; Ren, K.; Liu, S. The Joint Effect of Surface Polarity and Concentration on the Structure and Dynamics of Acetonitrile Solution: A Molecular Dynamics Simulation Study. *Phys. Chem. Chem. Phys.* **2020**, *22*, 10322–10334.
71. Cabaleiro-Lago, E. M.; Ríos, M. A. Intermolecular Potential for Acetonitrile Based on ab Initio Calculations. *Mol. Phys.* **1999**, *96*, 309–321.
72. Grabuleda, X.; Jaime, C.; Kollman, P. A. Molecular Dynamics Simulation Studies of Liquid Acetonitrile: New Six-Site Model. *J. Comput. Chem.* **2000**, *21*, 901−908.
73. Guàrdia, E.; Pinzón, R.; Casulleras, J.; Orozco, M.; Luque, F. J. Comparison of Different Three-Site Interaction Potentials for Liquid Acetonitrile. *Mol. Simul.* **2001**, *26*, 287–306.
74. Price, M. L. P.; Ostrovsky, D.; Jorgensen, W. L. Gas-Phase and Liquid-State Properties of Esters, Nitriles, and Nitro Compounds with the OPLS-AA Force Field. *J. Comput. Chem.* **2001**, *22*, 1340−1352.
75. Wick, C. D.; Stubbs, J. M.; Rai, N.; Siepmann, J. I. Transferable Potentials for Phase Equilibria. 7. Primary, Secondary, and Tertiary Amines, Nitroalkanes and Nitrobenzene, Nitriles, Amides, Pyridine, and Pyrimidine. *J. Phys. Chem. B* **2005**, *109*, 18974−18982.
76. Nikitin, A. M.; Lyubartsev, A. P. New Six-Site Acetonitrile Model for Simulations of Liquid Acetonitrile and Its Aqueous Mixtures. *J. Comput. Chem.* **2007**, *28*, 2020−2026.
77. Albertí, M.; Amat, A. De Angelis, F.; Pirani, F. A Model Potential for Acetonitrile: from Small Clusters to Liquid. *J. Phys. Chem. B* **2013**, *117*, 7065−7076.
78. Deublein, S.; Metzler, P.; Vrabec, J.; Hasse, H. Automated Development of Force Fields for the Calculation of Thermodynamic Properties: Acetonitrile as a Case Study. *Mol. Simul.* **2013**, *39*, 109−118.
79. Alvarez, H. A.; Llerena Suster, C.; McCarthy, A. N. Consistent Acetonitrile Molecular Models for Both Standard and Computationally Efficient Molecular Dynamics Studies. *Asian J. Comp. Inf. Syst.* **2014**, *2*, 49−62.
80. Orhan, M. Dielectric and Transport Properties of Acetonitrile at Varying Temperatures: A Molecular Dynamics Study. *Bull. Kor. Chem. Soc.* **2014**, *35*, 1469−1478.
81. Kowsari, M. H.; Tohidifar, L. Systematic Evaluation and Refinement of Existing All-Atom Force Fields for the Simulation of Liquid Acetonitrile. *J. Comput. Chem.* **2018**, *39*, 1843−1853.

82. Hernández-Cobos, J.; Martínez, J. M.; Pappalardo, R. R.; Ortega-Blake, I.; Sánchez Marcos, E. A General Purpose Acetonitrile Interaction Potential to Describe Its Liquid, Solid and Gas Phases. *J. Mol. Liq.* **2020**, *318*, 113975.
83. Plimpton, S. Fast Parallel Algorithms for Short-Range Molecular Dynamics. *J. Comput. Phys.* **1995**, *117*, 1−19.
84. Martínez, L.; Andrade, R.; Birgin, E. G.; Martínez, J. M. PACKMOL: A Package for Building Initial Configurations for Molecular Dynamics Simulations. *J. Comput. Chem.* **2009**, *30*, 2157−2164.
85. Frenkel, D.; Smit, B. *Understanding Molecular Simulation: From Algorithms to Applications*, 2nd ed.; Academic Press: London, 2002.
86. Arnold, O.; Bilheux, J. C.; Borreguero, J. M.; Buts, A.; Campbell, S. I.; Chapon, L.; Doucet, M.; Draper, N.; Ferraz Leal, R.; Gigg, M. A.; Lynch, V. E.; Markvardsen, A.; Mikkelson, D. J.; Mikkelson, R. L.; Miller, R.; Palmen, K.; Parker, P.; Passos, G.; Perring, T. G.; Peterson, P. F.; Ren, S.; Reuter, M. A.; Savici, A. T.; Taylor, J. W.; Taylor, R. J.; Tolchenov, R.; Zhou, W.; Zikovsky, J. Mantid—Data Analysis and Visualization Package for Neutron Scattering and μ SR Experiments. *Nucl. Instrum. Methods Phys. Res. A* **2014**, *764*, 156−166.
87. Richard, D.; Ferrand, M.; Kearley, G. J. Analysis and Visualisation of Neutron-Scattering Data. *J. Neutron Res.* **1996**, *4*, 33−39.
88. Schober, H. An Introduction to the Theory of Nuclear Neutron Scattering in Condensed Matter. *J. Neutron Res.* **2014**, *17*, 109−357.
89. Schober, H.; Tölle, A.; Renker, B.; Heid, R.; Gompf, F. Microscopic Dynamics of AC_{60} Compounds in the Plastic, Polymer, and Dimer Phases Investigated by Inelastic Neutron Scattering. *Phys. Rev. B* **1997**, *56*, 5937−5950.
90. Bée, M. *Quasielastic Neutron Scattering: Principles and Applications in Solid State Chemistry, Biology and Materials Science*; Adam Hilger: Bristol, 1988.
91. Keen, D. A. A Comparison of Various Commonly Used Correlation Functions for Describing Total Scattering. *J. Appl. Crystallogr.* **2001**, *34*, 172−177.
92. Hansen, J.-P.; McDonald, I. R. *Theory of Simple Liquids: with Applications to Soft Matter*, 4th ed.; Academic Press: London, 2013.

93. Steiner, T.; Desiraju, G. R. Distinction Between the Weak Hydrogen Bond and the van der Waals Interaction. *Chem. Commun.* **1998**, 891−892.
94. Elola, M. D.; Ladanyi, B. M. Molecular Dynamics Study of Polarizability Anisotropy Relaxation in Aromatic Liquids and Its Connection with Local Structure. *J. Phys. Chem. B* **2006**, *110*, 15525−15541.
95. Headen, T. F.; Howard, C. A.; Skipper, N. T.; Wilkinson, M. A.; Bowron, D. T.; Soper, A. K. Structure of π-π Interactions in Aromatic Liquids. *J. Am. Chem. Soc.* **2010**, *132*, 5735−5742.
96. Asthana, B. P.; Deckert, V.; Shukla, M. K.; Kiefer, W. Isotopic Dilution Study of Self-Association in (CH_3CN + CD_3CN) Mixture by Scanning Multichannel Raman Difference Technique and ab-Initio Calculations. *Chem. Phys. Lett.* **2000**, *326*, 123−128.
97. Jorgensen, W. L.; Maxwell, D. S.; Tirado-Rives, J. Development and Testing of the OPLS All-Atom Force Field on Conformational Energetics and Properties of Organic Liquids. *J. Am. Chem. Soc.* **1996**, *188*, 11225−11236.
98. Torquato, S. Statistical Description of Microstructures. *Annu. Rev. Mater. Res.* **2002**, *32*, 77−111.
99. Canongia Lopes, J. N. A.; Pádua, A. A. H. Nanostructural Organization in Ionic Liquids. *J. Phys. Chem. B* **2006**, *110*, 3330−3335.
100. Enjalbert, R.; Galy, J. CH_3CN: X-ray Structural Investigation of a Unique Single Crystal. $\beta \rightarrow \alpha$ Phase Transition and Crystal Structure. *Acta Crystallogr. B* **2002**, *58*, 1005−1010.
101. Lovas, F. J. Microwave Spectral Tables : II. Triatomic Molecules. *J. Phys. Chem. Ref. Data* **1978**, *7*, 1445−1750.
102. Pochan, J.; Shoemaker, R. L.; Stone, R. G.; Flygare, W. H. Molecular *g* Values, Magnetic Susceptibility Anisotropies, Diamagnetic and Paramagnetic Susceptibilities, Second Moment of the Charge Distribution, and Molecular Quadrupole Moments of H_3CCN and H_3CNC*. *J. Chem. Phys.* **1970**, *52*, 2478, 2478−2484.
103. Battaglia, M. R.; Buckingham, A. D.; Williams, J. H. The Electric Quadrupole Moments of Benzene and Hexafluorobenzene. *Chem. Phys. Lett.* **1981**, *78*, 421−423.
104. de Luca, G.; Russo, N.; Sicilia, E.; Toscano, M. Molecular Quadrupole Moments, Second Moments, and Diamagnetic Susceptibilities Evaluated using the Generalized Gradient

Approximation in the Framework of Gaussian Density Functional Method. *J. Chem. Phys.* **1996**, *105*, 3206−3210.

105. Gacesa, M.; Byrd, J. N.; Smucker, J.; Montgomery, Jr., J. A.; Côté, R. Photoassociation of Ultracold Long-Range Polyatomic Molecules. *Phys. Rev. Res.* **2021**, *3*, 023163.
106. Maroulis, G. *Ab Initio* Determination of the Electric Multipole Moments and Static (Hyper)polarizability of HCCX, X = F, Cl, Br, and I. *J. Comput. Chem.* **2003**, *24*, 443−452.
107. Rodgers, J. M.; Ichiye, T. Multipole Moments of Water Molecules and the Aqueous Solvation of Monovalent Ions. *J. Mol. Liq.* **2017**, *228*, 54−62.
108. Richardi, J.; Fries, P. H.; Krienke, H. Influence of the Intermolecular Electrostatic Potential on Properties of Polar Polarizable Aprotic Solvents. *Mol. Phys.* **1999**, *96*, 1411−1422.
109. Hawlicka, E.; Grabowski, R.; Reimschüssel, W. Self-Diffusion and Conductance of Acetonitrile-Water Solutions of Tetraethylammonium Iodide. *Ber. Bunsenges. Phys. Chem.* **1990**, *94*, 158−162.
110. Hertz, H. G.; Leiter, H. Hydrophobic Interactions in Aqueous Mixtures of Methanol, Ethanol, Acetonitrile, and Dimethyl-Formamide. *Z. Phys. Chem. (Munich)* **1982**, *133*, 45−67.
111. Hurle, R. L.; Woolf, L. A. Self-Diffusion in Liquid Acetonitrile under Pressure. *J. Chem. Soc., Faraday Trans. 1* **1982**, *78*, 2233−2238.
112. Hawlicka, E. Acetonitrile-Water Solutions of Sodium Halides: Viscosity and Self-Diffusion of CH_3CN and H_2O. *Z. Naturforsch.* **1988**, *43a*, 769−773.
113. Holz, M.; Mao, X.; Seiferling, D.; Sacco, A. Experimental Study of Dynamic Isotope Effects in Molecular Liquids: Detection of Translation-Rotation Coupling. *J. Chem. Phys.* **1996**, *104*, 669−679.
114. Connell, M. A.; Bowyer, P. J.; Adam Bone, P.; Davis, A. L.; Swanson, A. G.; Nilsson, M.; Morris, G. A. Improving the Accuracy of Pulsed Field Gradient NMR Diffusion Experiments: Correction for Gradient Non-Uniformity. *J. Magn. Reson.* **2009**, *198*, 121−131.
115. Kovacs, H.; Kowalewski, J.; Maliniak, A.; Stilbs, P. Multinuclear Relaxation and NMR-Self-Diffusion Study of the Molecular Dynamics in Acetonitrile-Chloroform Liquid Mixtures. *J. Phys. Chem.* **1989**, *93*, 962−969.

116. Impey, R. W.; Madden, P. A.; McDonald, I. R. Hydration and Mobility of Ions in Solution. *J. Phys. Chem.* **1983**, *87*, 5071−5083.
117. Redner, S. *A Guide to First-Passage Processes*, 1st ed.; Cambridge University Press: Cambridge, 2001.
118. Hartkamp, R.; Coasne, B. Structure and Transport of Aqueous Electrolytes: From Simple Halides to Radionuclide Ions. *J. Chem. Phys.* **2014**, *141*, 124508.
119. Cazade, P.-A.; Hartkamp, R.; Coasne, B. Structure and Dynamics of an Electrolyte Confined in Charged Nanopores. *J. Phys. Chem. C* **2014**, *118*, 5061−5072.
120. Laage, D.; Hynes, J. T. On the Residence Time for Water in a Solute Hydration Shell: Application to Aqueous Halide Solutions. *J. Phys. Chem. B* **2008**, *112*, 7697−7701.
121. Valandrini, V.; Pellegrini, E.; Calligari, P.; Hinsen, K.; Kneller, G. R. nMoldyn – Interfacing Spectroscopic Experiments, Molecular Dynamics Simulations and Models for Time Correlation Functions. *Collection SFN* **2011**, *12*, 201−232.
122. Hugouvieux, V.; Farhi, E.; Johnson, M. R.; Juranyi, F.; Bourges, P.; Kob, W. Structure and Dynamics of *l*-Ge: Neutron Scattering Experiments and *ab initio* Molecular Dynamics Simulations. *Phys. Rev. B* **2007**, *75*, 104208.
123. Bopp, T. T. Magnetic Resonance Studies of Anisotropic Molecular Rotation in Liquid Acetonitrile-d_3. *J. Chem. Phys.* **1967**, *47*, 3621−3626.
124. Behrens, M.; Fröchtenicht, R.; Hartmann, M.; Siebers, J.-G.; Buck, U.; Hagemeister, F. C. Vibrational Spectroscopy of Methanol and Acetonitrile Clusters in Cold Helium Droplets. *J. Chem. Phys.* **1999**, *111*, 2436−2443.